Hydrogen in Disordered Titania: Connecting Local Chemistry, Structure, and Stoichiometry through Accelerated Exploration

Journal:	*Journal of Materials Chemistry A*
Manuscript ID	TA-ART-09-2022-007075.R2
Article Type:	Paper
Date Submitted by the Author:	26-Jan-2023
Complete List of Authors:	Chapman, James; Boston University, Mechanical Engineering Kweon, Kyoung; Lawrence Livermore National Laboratory, Zhu, Yakun; Lawrence Livermore National Laboratory Bushick, Kyle; University of Michigan Bayu, L.; Lawrence Livermore National Laboratory, Colla, Christopher; Los Alamos National Laboratory Mason, Harris; Lawrence Livermore National Laboratory, Goldman, Nir; Lawrence Livermore National Laboratory, Materials Science Division Keilbart, Nathan; Lawrence Livermore National Laboratory Qiu, S. Roger; Lawrence Livermore National Laboratory, Heo, Tae Wook; Lawrence Livermore National Laboratory, Materials Science Division Rodriguez, Jennifer; Lawrence Livermore National Laboratory Wood, Brandon; Lawrence Livermore National Laboratory

Hydrogen in Disordered Titania: Connecting Local Chemistry, Structure, and Stoichiometry through Accelerated Exploration

James Chapman *[1,4], Kyoung E. Kweon †[1], Yakun Zhu‡[1], Kyle Bushick[1,3], Leonardus Bimo Bayu Aji[1], Christopher A. Colla[1], Harris Mason[1], Nir Goldman[1,2], Nathan Keilbart[1], S. Roger Qiu[1], Tae Wook Heo[1], Jennifer Rodriguez[1], and Brandon C. Wood§[1]

[1] *Materials Science Division, Lawrence Livermore National Laboratory, Livermore, CA, USA*
[2] *Department of Chemical Engineering, University of California, Davis, California 95616, United States*
[3] *Department of Materials Science and Engineering, University of Michigan, Ann Arbor, Michigan 48109, United States*
[4] *Department of Mechanical Engineering, Boston University, Boston, Massachusetts 02215, United States*

January 26, 2023

Abstract

Hydrogen incorporation in native surface oxides of metal alloys often controls the onset of metal hydriding, with implications for materials corrosion and hydrogen storage. A key representative example is titania, which forms as a passivating layer on a variety of titanium alloys for structural and functional applications. These oxides tend to be structurally diverse, featuring polymorphic phases, grain boundaries, and amorphous regions that generate a disparate set of unique local environments for hydrogen. Here, we introduce a workflow that can efficiently and accurately navigate this complexity. First, a machine learning force field, trained on ab initio molecular dynamics simulations, was used to generate amorphous configurations. Density functional theory calculations were then performed on these structures to identify local oxygen environments, which were compared against experimental observations. Second, to classify subtle differences across the disordered configuration space, we employ a graph-based sampling procedure. Finally, local hydrogen binding energies and hopping kinetics are computed using exhaustive density functional theory calculations on representative configurations. We leverage this methodology to show that hydrogen binding energetics are described by local oxygen coordination, which in turn is affected by stoichiometry, and form the basis of hopping kinetics and diffusion. Together these results imply that hydrogen incorporation and transport in TiO_x can be tailored through compositional engineering, with implications for improving performance and durability of titanium-derived alloys in hydrogen environments.

Introduction

Ultimately, corrosion is a thermodynamically driven process that affects all metal/metal-oxide systems and alloys, usually through one of several mechanisms, such as hydrogen embrittlement, galvanic processes, or oxidation [1]. Hydrogen embrittlement in particular can cause severe and dangerous damage due to the spontaneous formation of metal hydrides. These reactions are sometimes pyrophoric, and the hydrides themselves are frequently dispersive powders that are highly toxic [2]. As a result, mitigation of this process has ramifications for a number of manufacturing efforts, including actinides processing [3], stainless steel reinforcement, etc.

---

[*] Corresponding Author, jc112358@bu.edu
[†] Corresponding Author, kweon1@llnl.gov
[‡] Corresponding Author, zhu15@llnl.gov
[§] Corresponding Author, wood37@llnl.gov

Typically, transition metals such as titanium are naturally covered with a protective oxide layer than inhibits embrittlement[4]. This protection is not permanent though, with chemical species such as oxygen and hydrogen eventually diffusing through the oxide and into the bulk metal/alloy [5, 6]. This sequence of events implies that the incubation (initiation) time, and ultimately failure, of the system is rate-limited by the ability of the corrosive chemical agents to permeate the oxide layer. Hydriding initiation thus most likely begins at this oxide surface, where hydrogen can diffuse through and attack the metal underbelly, thereby starting the conversion of titanium into TiH_2. However, there is still a question of how hydrogen is transported from the surface into the metal itself. The oxide layer is likely polycrystalline [7], with a number of unique and complex atomic environments existing between the oxide surface and the underlying metal, including grain boundaries, nano/microscale defects such as voids and cracks, and the interface region between the oxide and metal/alloy [8–13]. There is speculation that thermodynamic driving forces exist that result in larger hydrogen concentration in the grain boundaries, which themselves are likely disordered and resemble amorphous phases[14]. These then become channels for mass transport to the metallic material underneath.

As a result, the lifetime of a given metal or alloy could be extended through control over the kinetics of key underlying hydrogen transport processes within the oxide. While the failure of materials under steady-state conditions can be predicted exceptionally well through the use of parameterized empirical models, the precursors to hydriding initiation are still poorly understood [15–18]. This initial stage of the embrittlement process is non-trivial, as its effects are likely coupled together with other complex phenomena (i.e., nucleation and growth of the metal hydride) in possibly complex and unintuitive ways. As no single methodology currently exists to explicitly explore diffusion through all aforementioned features within the oxide layer under dynamic conditions, a piece-meal approach must be taken to understand how hydrogen behaves within each structural environment [19–21].

In this work we investigate the thermodynamics of hydrogen binding within the grain boundary regions of TiO_x using a combination of density functional theory (DFT), a machine learning force field, and a graph theoretical structure characterization technique. As previously stated, amorphous titania was chosen as a surrogate for grain boundaries. Explicitly simulating hydrogen diffusion within the amorphous phase under dynamic conditions is non-trivial, as the size and time requirements are outside of the realm of DFT, and classical models have difficult adequately capturing the electronic effects that determine hydrogen binding [22, 23].

Therefore, we adopt a three-step computational workflow to overcome these challenges: (1) machine learning force field classical molecular dynamics simulations to explore vast regions of the amorphous phase space, (2) graph-theory driven structure characterization to identify and down-select representative structures, and (3) density functional theory calculations on the sampled configurations, with hydrogen inserted in the system, to obtain the hydrogen binding energy with a high level of fidelity. This pipeline allows for the "best-of-both-worlds", where fast and efficient molecular dynamics (MD) simulations can be performed to generate a practically unlimited number of configurations and expensive but accurate DFT calculations can provide a reliable estimation to the spectrum of possible hydrogen binding energies present with the amorphous phase space.

The rest of the paper is as follows. We begin by providing a detailed understanding of the various methodological aspects of our computational and experimental procedures. We then provide a detailed description of the atomic structure of amorphous titania using both experiments and simulations. We show that our simulation framework, which combines nuclear magnetic resonance (NMR), MD, and graph theory, can accurately link the characterization of local oxygen environments to experimental NMR observations. Our MD simulations are also used to understand the effect of oxygen concentration on the likelihood of finding specific oxygen coordination environments within an amorphous sample, and use this information to validate the experimental characterization. We then give a detailed description of the DFT calculated hydrogen binding energies for both stoichiometric and non-stoichiometric amorphous titania. Next, we calculate hydrogen hopping kinetics via nudged elastic band (NEB) calculations for specific hopping pathways. Finally, we discuss how the observations gathered from this work give insight into how structural features such as the oxygen concentration could ultimately be used to tailor properties such as hydrogen diffusion and permeation.

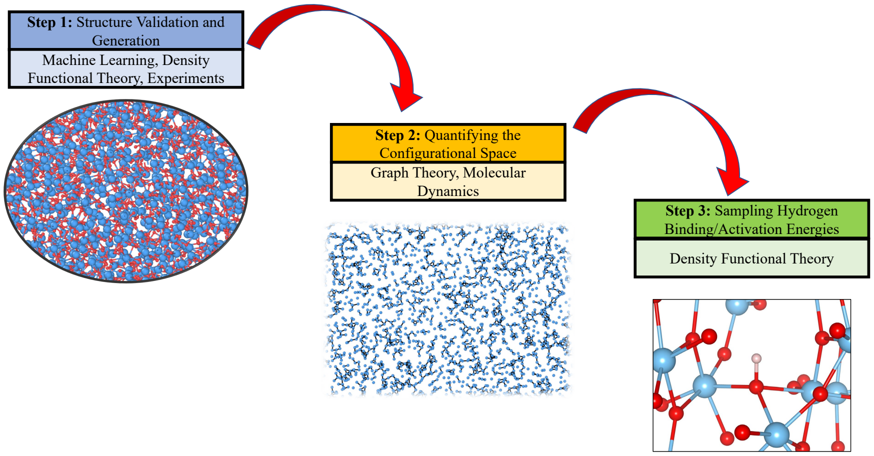

Figure 1: Step 1: the atomic structure of amorphous titania is generated both via ab initio and machine learning-driven MD simulations and experimental synthesis. This atomic structure is then validated through the use of NMR experiments and simulations. Step 2: bounds on the amorphous phase space are quantified by employing a graph characterization technique on the machine learning-driven MD simulations, providing an accurate description of the amorphous configurational space. Step 3: hydrogen binding and hopping activation energies are calculated using DFT in a high throughput manner.

Methods

Computational Methods

Computational workflow

The computational workflow used in this work employs a 3-step approach, in which long time-scale MD simulations are performed with an atomic force neural network (AFNN) and then a characterized, geometrically, with a graph-based order parameter. Representative structures are then down-selected using a combination of K-means clustering and stochastic random sampling. DFT calculations are then performed to obtain the hydrogen binding energy of the down-selected structures. This workflow combines the advantages of each methodology: (1) machine learning force fields can explore vast regions of the configurational space not attainable with DFT, (2) graph theory provides a physics-informed phase space characterization, making sampling intuitive and efficient, and (3) high-fidelity DFT binding energy calculation ensures that the resulting energy distributions are accurate and reliable. Fig. 1 provides a visual depiction of this computational workflow.

Electronic structure details

DFT calculations were performed using the VASP package [24] with projector augmented wave (PAW) pseudo potentials [25]. As valence electrons, we considered the $3p^6 3d^2 4s^2$ electron configuration for Ti and $2s^2 2p^4$ for O, respectively. The PBE exchange-correlation functional revised for solids (PBEsol) [26] was used to compute structural properties of bulk titania more accurately [27].

Ab initio molecular dynamics

To generate amorphous structures, the melt-quench method was applied for TiO_2 (having 72 Ti and 144 O atoms) and $TiO_{1.88}$ (having 72 Ti and 135 O atoms) systems using AIMD simulations [28–30]. Starting from 72 Ti and 144 O atoms in a cubic cell with two different crystalline atomic configurations (rutile and anatase), the randomized TiO_2 structures were generated by very high temperature AIMD at 5000 K in the canonical (NVT) ensemble for 10 ps with a 2 fs time step; similarly, two randomized $TiO_{1.88}$ structures were created from crystalline $Ti_{72}O_{144}$ by removing 9 O atoms. The randomized structures are cooled to the liquid temperature of 2250 K during 2 ps and subsequently equilibrated at 2250 K for 5 ps in NVT. After that, two snapshots were taken every 5 ps from further dynamics at 2250 K within the microcanonical (NVE) ensemble to improve statistical distribution of local and independent melt structures. Note that the experimental density of 3.21 g/cm^3 for the liquid TiO_2 [31] was used for the simulated liquid model at 2250 K (the same density of 3.21g/cm^3 is used for the $TiO_{1.88}$ at 2250 K).

The final structures were obtained by taking each melted snapshot and quenching to 300 K with a cooling rate of 19.5 K/ps, for an overall quenching time of 100 ps. Here, the quench process was performed using the NVT ensemble, while the density of system was rescaled every 8 ps (equivalent to 156 K) to account realistic density change of the liquid [31, 32] during the quenching as suggested by Mavračić et. al [28]. Finally, the quenched structures were equilibrated at 300 K for 10 ps under NVT conditions, using DFT+U calculations (as will be discussed later), to ensure that the structure is fully optimized under ambient pressure. For each TiO_2 and $TiO_{1.88}$, four different independent structures were obtained, while the density at 300K is further optimized, resulting in the average final densities of 3.72 g/cm^3 for TiO_2 and 3.55 g/cm^3 for $TiO_{1.88}$, respectively; note that with energy variations within the structures, only three structures with lower energies were taken for additional calculations. For all AIMD simulations, a time step of 1 fs was employed unless mentioned otherwise. For all NVT simulations, the Nosé-Hoover thermostat was used.

Ab initio NMR details

The isotropic chemical shift (δ_{iso}) for O sites is computed as $\delta_{iso} = \delta_{cal} + \delta_{ref}$, where δ_{cal} is the calculated chemical shift via the linear response method in VASP and δ_{ref} is the chemical shift for the reference compound [33–36]. We included the contribution from the core electrons as well as the valence electrons to obtain δ_{cal}. In this work, δ_{ref} is determined by aligning δ_{cal} for O in anatase to the corresponding experimental δ_{iso} (557 ppm) [37]. To accurately calculate the variation in the electronic structures within the linear response approach, a higher energy cutoff of 600 eV and denser 2x2x2 Monkhorst-Pack k-grid were used for the 96 atom supercell. With 400 different amorphous models, a total of 30,000 δ_{iso} datapoints for O sites were collected, which is large enough to capture the correlation between δ_{iso} for O sites and their coordination environment. All NMR calculations were performed on AFNN-generated structures, without hydrogen, as described in the following sections.

Ab initio structure optimization

After the melt-quenching AIMD simulations, structural optimization for the amorphous TiO_x ($x = 2$ or 1.88) was carried out using spin-polarized DFT calculations to include the electron spin polarization with the plane-wave energy cutoff of 450 eV. We also employed DFT+U within Dudarev's approach [38] to correct the electronic self-interaction error for the localized 3d states, which becomes crucial to accurately describe structural and electronic properties of oxygen deficient titania with H interstitials and/or O vacancies [39–41]; a value of Hubbard U = 4 eV is applied for all Ti 3d states [35]. The Brillouin zone integration is approximated using a single k-point (Γ-point), which could be sufficient for the reasonably large supercells (containing 72 TiO_x formula units) of insulating systems with a relatively small computational cost. All structures were relaxed until the force on each atom is less than 0.02 eV/$\AA$.

Ab initio hydrogen hopping kinetics

Upon hydrogen insertion, nudged elastic band calculations [42] were performed, using the TST package in VASP. First, structural optimizations for the initial and final 96-atom amorphous TiO_2 structures were carried out. Spin-polarized DFT calculations were used to include the electron spin polarization with the plane-wave energy cutoff of 450 eV. We also employed DFT+U within Dudarev's approach [38] to correct the electronic self-interaction error for the localized 3d states, which becomes crucial to accurately describe structural and electronic properties of oxygen deficient titania with H interstitials and/or O vacancies [39–41]; a value of Hubbard U = 4 eV is applied for all Ti 3d states [35]. The Brillouin zone integration is approximated using a single k-point (Γ-point). All structures were relaxed until the force on each atom was less than 0.03 eV/$\AA$ and the total energy of the system had converged to a tolerance of 10^{-5} eV.

During all NEB calculations, a spring constant of -3 eV/$\AA^2$ was used. Three images, outside of the initial and final configurations were used. The climbing image formalism was employed too all NEB calculations. The NEB routine was terminated when the force on each atom was less than 0.03 eV/$\AA$ and the total energy of the system had converged to a tolerance of 10^{-7} eV. The cell volume remained fixed during the NEB relaxations.

Atomic force neural network details

In this work, atomic forces are learned by establishing a mapping between the atomic features and their respective atomic force components using a deep neural network (NN). The AFNN framework was designed based on previous works regarding machine learning force matching schemes [43–45]. As there are multiple species present, two AFNNs are employed to independently predict the atomic forces acting on a given chemical element: one AFNN for Ti, and another for O. A visual description of this arrangement can be found in the supplemental information. The NN architecture of both AFNNs employs an input layer containing a neuron count equal to the number of atomic features, one hidden layer containing a neuron count equal to the input layer, a second hidden layer containing a neuron count equal to four times that of the input layer, and a single output that maps to a given force component. Therefore, each atom will make three independent NN predictions to account for the x, y, and z atomic force components. Each AFNN employed the $tanh$ activation function throughout all hidden layer neurons, due to its symmetry about $x = 0$, which matches the expected symmetry of the atomic forces with respect to the atomic features. A bias vector is also associated with each layer in the AFNN, helping to control the values passed into each neuron's activation function.

During the AFNN model's training phase only TiO_2 was used to train the model (216-atom DFT data), while the non-stoichiometric DFT data ($TiO_{1.88}$) was used to validate the model's ability to extrapolate to unseen environments. 75% of the reference data was sampled using the K-Means clustering [46] algorithm within the atomic feature space (using 100 randomly initialized clusters). After the K-means clusters had been optimized, training data was randomly sampled from within each cluster until the desired number of training points had been met. The remaining 25% split equally into validation and test sets. 10000 epochs were used to ensure convergence in the model's predictions, along with the Adamax optimization algorithm [47]. More details regarding the AFNN training can be found in the supplemental information.

Classical structure generation details

All structures used in this work were generated via MD using the AFNN described in the previous sections, using the LAMMPS [48] software. A 96-atom crystal structure in the rutile phase was used as the initial configuration. MD was then performed at 4000K to superheat and liquify the rutile crystal. The cell shape was then slowly modified, manually, until the lattice vectors reached a cubic configuration. The system temperature was then brought down to 2250K, a temperature previously reported as showing the existence of the amorphous phase [31]. The lattice vectors were again altered, isotropically, until the volume-to-atom ratio reached 12.40 $\frac{\AA^3}{atom}$, which was obtained from previously calculated values [28–30]. The system was then equilibrated at 2250K using the finalized system volume. A 25ns MD simulation was then performed in the NVT ensemble at 2250K to generate a large dataset of possible amorphous configurations.

A larger system, containing 1944 atoms was also used to justify the use of the 96-atom configurations by observing that both trajectories live within the same region of phase space, a point that is discussed later. The same procedure described above was used to generate the 1944-atom structures. However, due to issues with the AFNN, the same density could not be attained for the 1944-atom system. Large voids opened within the configuration, potentially due to periodic box effects. Therefore, the 1944-atom system was slightly compressed to 11.74 $\frac{\AA^3}{atom}$, which was attained by minimizing the differences in the radial distribution function between the 1944-atom and 96-atom trajectories. While the use of the slightly compressed system may leave out potential periodic size effects at the correct density, the matching of the RDF ensures that a direct comparison can still be made between the two trajectories, as properties such as the oxygen coordination number and nearest neighbor distances will remain nearly identical.

For both the 96-atom and 1944-atom trajectories, several non-stoichiometric cases were also considered: (a) $TiO_{1.85}$, $TiO_{1.9}$, $TiO_{1.95}$ for the 1944-atom system, and (b) $TiO_{1.88}$ for the 96-atom system. These trajectories were generated by first taking the perfect amorphous system and removing the corresponding number of oxygen atoms at random. MD was then performed at 2250K in the NVT ensemble with the oxygen deficient system for 25ns. All non-stoichiometric MD trajectories were generated using the same volume as their respective stoichiometric cases.

For the 96-atom configurations hydrogen was also inserted into the $TiO_{1.88}$ and TiO_2 systems in order to calculate the hydrogen binding energy. Using the down-selected sites described earlier, 5 random oxygen atoms were chosen to form an O-H bond from each configuration such that no two oxygen atoms of the 5 initial sites were closer than 3Å. In the event that any pair of oxygen atoms were closer than 3Å, one of the two was ignored. Any duplicate oxygen sites were also removed during this process. Out of all initial configurations, no snapshot has less than 3 possible hydrogen sites, resulting in 6,865 and 7,556 TiO_xH structures for $x = 2$ and 1.88 respectively. All TiO_xH configurations were then relaxed using DFT in order to obtained the final configuration.

Graph-based atomic structure characterization

The diversity and complexity of the amorphous titania phase space necessitates the efficient and reliable characterization of its atomic structures. In this work, we employ a graph-based methodology, Graph Coordination Network (GCN) [49], to classify local pairwise atomic environments contained within a configuration of atoms. Fig. S5 provides a graphical visualization of how the GCNs are constructed within amorphous titania. These weighted networks encode radial distances as $1/r_{ij}^2$, where i and j are the atomic IDs of two atoms. This information is then mapped into a graph order parameter (SGOP), which encodes the connectivity and shape of the graph by leveraging information contained in the set of unique degrees over the graph. Several SGOPs, defined by their radial cutoff distances, are finally grouped together within a single vector, referred to as the Vector Graph Order Parameter (VGOP). Further information regarding the theory behind this methodology can be found in the supplemental information.

Experimental Methods

Material synthesis

Titanium isopropoxide (obtained from Aldrich) was mixed with 17O (35-40%) labeled demineralized water [50] (obtained from Cambridge Isotope Lab, Inc) at a molar ratio of 1:4. The liquid mixture was stirred to accelerate precipitation. The resulting white precipitate was subsequently left to dry in a furnace in air and at 100 °C for 3 days prior to analysis.

Characterization and analysis

A Bruker D8 DISCOVER X-ray diffractometer (XRD) was used for phase analysis with a step size of 0.01°/step, a dwell time of 2 s/step, and a scan range of $20 - 80^{\circ}$. Microstructure analysis was carried out using a FEI 80-300 Titan transmission electron microscope (TEM), equipped with a four-detector energy dispersive x-ray spectroscopy (EDS) system known as ChemiSTEMTM. The sample was prepared by spreading powders on a Cu grid.

Titanium oxide (TiO_x) films were prepared by pressing the TiO_x powders onto planar carbon substrate. Rutherford backscattering spectrometry (RBS) was employed to measure the compositional depth profile in the TiO_x films. Samples were bombarded with a 2 MeV 4He+ ion beam incident between 0 and 10 to the sample surface (to minimize ion channeling in textured films) and scattered into a detector at 165° from the incident beam direction. The analysis of RBS spectra was performed with the RUMP code [51, 52]. with the stoichiometry of O/Ti=2±0.2 the simulation yields the best fitting to the measured data. The best fit to the experimental data is obtained with O/Ti = 2.

XPS was performed on a PHI Quantum 2000 Scanning ESCA Microprobe using a monochromated Al Ka x-rays (1486.6 eV). Calibration was performed using Au $4f_{7/2}$ at 84.1 eV and the take-off angle was 60°. The X-ray spot size was around 200 µm. Survey spectra for each sample were recorded using a pass energy of 100 eV and a step size of 1 eV [53], and high-resolution spectra of each sample for the C 1s, O1s, Ti 2p, and Ti 3p regions were recorded with a pass energy of 20 eV and a step size of 0.1 eV. The C1s peak at 284.8 eV for adventitious carbon was used as a reference for all spectra [53]. High resolution spectra were

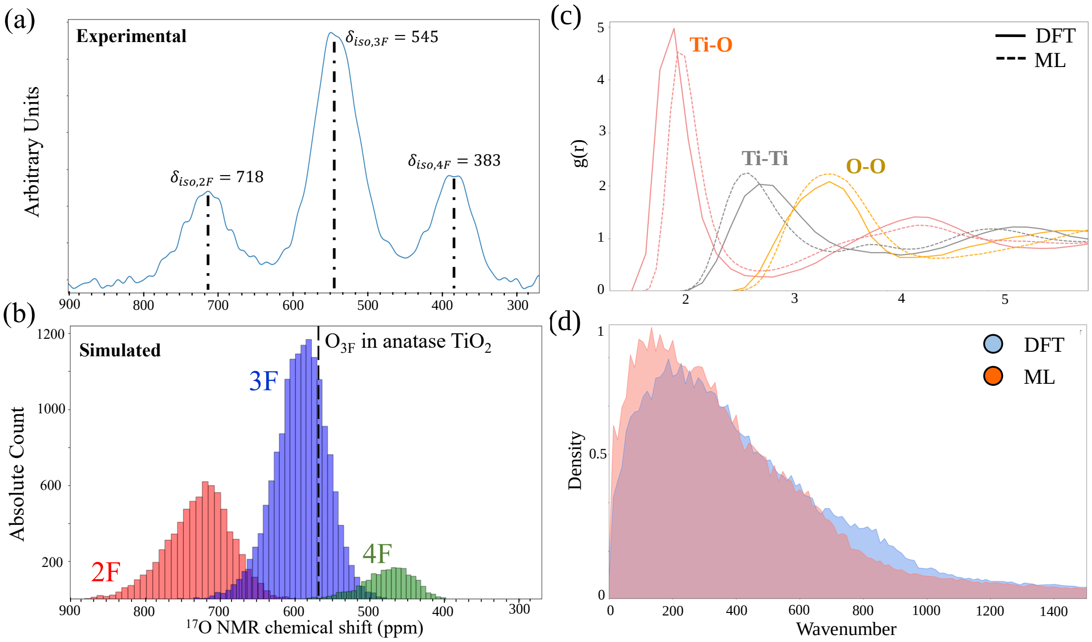

Figure 2: (a) Experimental NMR spectra calculated using a prepared amorphous titania sample. (b) Distribution of computed isotropic chemical shift (δ_{iso}) for O in a-TiO_2. Colors define δ_{iso} for different oxygen coordination numbers, as defined by the corresponding labels in (b). The dashed vertical line represents the δ_{iso} for a 3F oxygen atom in crystalline anatase TiO_2. (c) Molecular dynamics derived time-averaged pair-correlation function of amorphous TiO_2 at T=2250K, for both DFT and the AFNN. The pair-correlation function is decomposed based on chemical species interactions (colors, with identifying labels). The AFNN is shown as the solid line, while DFT is given as a dashed line. (d) The vibrational density of states, derived from molecular dynamics simulations at T=2250K, for DFT (light blue) and the AFNN (pink). In both scenarios, DFT calculations were performed on 216 atoms, while AFNN simulations were performed using 1944 atoms.

curve-fitted using Multipak 9.6.15 using a Shirley background subtraction. Gaussian-Lorentzian peaks were used for curve fitting [53].

Solid-state 17O and 1H NMR experiments were conducted on a Bruker Avance III NMR spectrometer at 600 MHz. Samples were loaded into 2.5mm NMR rotors and spun at 50kHz. Tap water was used as a chemical shift reference for 17O and TMS for 1H. NMR spectra fitting and quantification was performed using the "dmfit" software package [54].

Software Tools

All DFT calculations were performed using the VASP software [24]. All AFNN MD simulations were performed using the LAMMPS software [48]. All atomistic visualizations were created using the OVITO software [55]. All plots were created using the Matplotlib software [56]. Fitted histograms shown in Fig. 5 were created using SciPy [57]. All PCA anlaysis were performed using the scikit-learn software [58]. Experimental NMR spectra fitting and quantification was obtained through the "dmfit" software [54]. High resolution spectra were curve-fitted using the Multipak software version 9.6.15.

Results

Generation and validation of amorphous TiO_2 structures

As a first step, it is critical to introduce a benchmark against which our model of disordered TiO_2 can be validated. Accordingly, we produced a representative sample of amorphous TiO_2 powders using a sol-gel method (see Experimental Methods for details). The sample was characterized using ^{17}O solid-state NMR, which provides a spectroscopic "fingerprint" that can also be directly computed from our computational representation (additional XPS measurements can be found in the Supporting Information). Figure 2(a) shows the experimentally measured ^{17}O NMR isotropic chemical shifts on the amorphous powder, in which three distinct peaks at 718 ppm, 545 ppm, and 383 ppm can be identified. This implies that three distinct oxygen environments exist within the disordered TiO_2 material, each of which should be reproduced in a properly generated model.

Next, we proceeded to generate a range of configurations that capture these same local environments in atomistic TiO_2 models. Because the range and complexity of the amorphous configurations requires an efficient method for computing atomic forces, we developed an AFNN to rapidly generate structures. A 1944-atom system was used to validate the AFNN against 216-atom DFT simulations (a comparison between DFT and AFNN results for identically sized 96-atom systems can be found in the Supporting Information). Figure 2 (c) shows AFNN and DFT predictions of the time-averaged RDF (decomposed into $i-j$ species interactions), calculated from MD simulations, and (d) vibrational density of states. Overall, the AFNN RDF is in good agreement with the DFT RDF, other than slight variations in the interatomic distances. It should be noted that the AFNN simulations cover a much larger region of the TiO_2 phase space than the DFT trajectories, which only contain a few hundred structures along a single trajectory. This, combined with the small difference in density, can explain the subtle shifts observed in the RDF.

The AFNN also shows good agreement with DFT in regard to the vibrational density of states over all calculated wavenumbers. Some disagreement does exist at small wavenumbers, with the larger density predicted by the AFNN indicating a slightly more diffuse system. This is corroborated by observing the diffusion constants of both Ti and O, predicted via the mean square displacement, which show errors of a factor of 1.5 and 1.8 for Ti and O respectively, when compared to DFT. These discrepancies, however, are minimal, and indicate that the AFNN can reliably predict the vibrational behavior TiO_2 at 2250K over a wide spectrum of atomic perturbations. It is also worth noting that errors in the predicted diffusion constant values can be quite high due to the limited simulation length of DFT, and agreement within a factor of two is more than acceptable.

A similar trend exists between the AFNN and DFT with respect to the local structure predicted for cases with lower oxygen concentrations (up to $TiO_{1.88}$), indicating that one can use the AFNN to reasonably predict the correct underlying atomic environments for a range of oxygen concentrations. Detailed calculations of the mean-square displacement calculated diffusion constants for both Ti and O can be found in the supplemental information, along with a comparison between DFT and the AFNN for the non-stoichiometric case of $TiO_{1.88}$.

Having validated the ability of the AFNN to reproduce DFT results, we generated roughly 400 different amorphous models (using the 96-atom amorphous structures generated via the AFNN's MD simulations), which gives a total of approximately 30,000 δ_{iso} local environments for O sites. The O isotropic chemical shift (δ_{iso}) for each oxygen site was computed, as shown in Fig. 2 (b). The results reproduce the same three-peak structure that was identified through experimental measurements. Unlike the experimental observations, our DFT NMR structure can be mapped back onto the oxygen coordination number as we have explicit atomistic structure as reference. Figure 2(b) shows the strong correlation between δ_{iso} for the O sites and their corresponding coordination environment. The distribution of δ_{iso} shows that it is strongly dependent on the O coordination number with the increasing δ_{iso} for the lower O coordination numbers.

This coordination-environment dependence exists because as one decreases the number of electron-donating Ti atoms (lowering the coordination number), the electron density at the O nucleus is reduced, which deshields the nucleus and results in a larger δ_{iso}. Note that the δ_{iso} of 557 ppm for a 3F O in bulk anatase [59] is within the range of chemical shift for the 3F O in our a-TiO_2 (500-700 ppm). The coordination dependent δ_{iso} for O was also observed from the solution ^{17}O NMR study of titanium polyoxoalkoxide complexes, which contain 2F (OTi_2), 3F (OTi_3), and 4F (OTi_4) groups and each of which distinctly gives

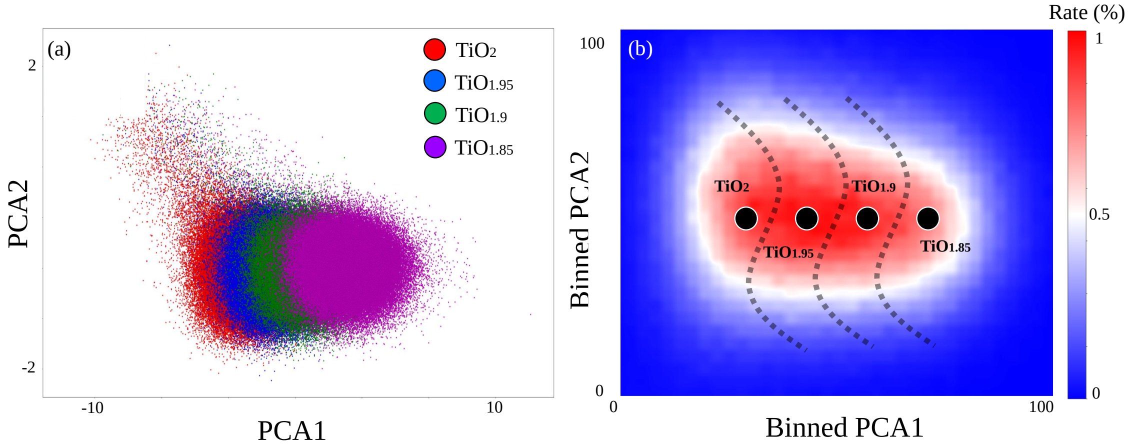

Figure 3: (a) PCA-decomposed TiO_x phase space, with colors representing varying oxygen concentrations. (b) 2D histograms of the PCA-decomposed TiO_x phase space, with occurrence rate (colors) overlayed as a third dimension. Occurrence rate is defined as the likelihood of a structure from a given PCA grid occurring in the overall phase space. Dashed lines in (b) provide visual context for the approximate boundary of each phase, where a bin contains greater than 50 % of a specific phase.

δ_{iso} of 650-850 ppm, 450-650 ppm, and 250-450 ppm, respectively [59].

The ranges in chemical shift for each major peak in Fig. 2 (a) and (b) suggest the presence of various O coordination environments in amorphous TiO_2, even within a specific coordination number (CN) (ex: many differnt types of 2F environments). Based on the calculated δ_{iso} in Fig. 2 (a), the experimental peaks at 718 ppm, 545 ppm and 383 ppm in Fig. 2 (b) are assigned to 2F, 3F, and 4F O sites, respectively. Note that for the 2F O coordination, the calculated δ_{iso} at 720 ppm corresponds well with the observed one, whereas there is slight overestimation of the calculated δ_{iso} for the 3F O sites at 585 ppm and 4F O sites at 460 ppm, respectively. Such minor discrepancies are common and can in principle be resolved by including an additional empirical scaling factor [36], but the current approach is sufficient for proper interpretation of the peak assignments. Overall, we confirm that the local coordination environment around O in our constructed amorphous TiO_2 models is highly comparable to that in the experimentally synthesized TiO_2. Quantification of the experimental peak areas reveals fractions of 14.78%, 39.15%, and 14.68%. for 2F, 3F, and 4F O respectively.

Exploration of the amorphous phase space

Here we use the 1,944 atom amorphous trajectories, generated by the AFNN, to analyze the local atomic geometries present across the vast phase space. We use the 1,944 atom systems to perform this analysis due to the increased number of local atomic sites present when compared to the 96 atom configurations. As described earlier when validating the AFNN, the 1,944 atom trajectories provide an excellent substitute when compared to DFT, and we do not expect the local atomic environments in 1,944 atom systems to deviate significantly from those present within the 96 atom structures.

Using the AFNN-generated 1,944 atom MD trajectories, the TiO_x phase space was characterized using the PCA decomposition of the VGOP features described earlier. Fig. 3(a) shows where various values of x, in TiO_x, lie within this configuration space. The VGOP shows a clear separation between each case considered in this work, with some overlap existing at the outskirts of each sub-space. The TiO_2 sub-space shares some overlap with the $TiO_{1.95}$ sub-space, but does not share any portion of the total space with another value of x. This makes sense intuitively, as one would expect the structures encountered during a dynamic trajectory to oscillate about some equilibrium point. As the underlying structure of TiO_2 and $TiO_{1.95}$ are similar, one would expect their oscillations to overlap at the fringes of their respective sub-spaces.

The ability to clearly distinguish between sub-spaces, in such a complex phase space, provides us with the ability to analyze these systems in more detail. For example, in Fig. 3(b), we can observe which part

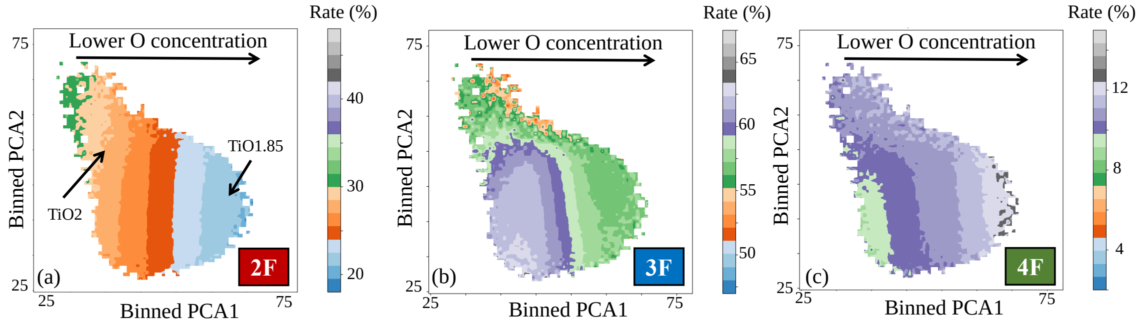

Figure 4: 2D histograms of the PCA-decomposed TiO_x phase space, with coordination number probabilities (colors) overlayed as a third dimension. Coordination number probabilities represent the likelihood of an atom having the specified coordination number within a structure that is contained within a given PCA grid. (a), (b), and (c) represent 2F, 3F, and 4F oxygen CN environments respectively.

of the phase space represents the equilibrium configurations contained within each sub-space, as well as the outlier regions. This provides us with the ability to estimate the probability of each region contained in the phase space from occurring at a given temperature. Here, we can see that the TiO_2 and $TiO_{1.85}$ sub-spaces exist in slightly different topological spaces, with TiO_2 experiencing larger oscillations about its equilibrium point than $TiO_{1.85}$. We can also observe a clear trend in that, as the oxygen concentration is decreased, the oscillations about a given chemistry's equilibrium point are reduced, implying a smaller overall phase space.

These oscillations provide insight into the size of a given oxygen concentration's portion of the overall phase space. For example, the $TiO_{1.85}$ phase space is visually more circular than the TiO_2 phase space, shown in Fig. 3. with a smaller radius from the center of the approximated clustering shown in 3 (b). This would seem to indicate that structures can deviate from the equilibrium configuration by a greater extent in TiO_2 than in $TiO_{1.85}$. These differences could play an important role in regard to H diffusion, as these oscillations about the equilibrium point may provide escape pathways, or trapping sites, that can ultimately make diffusion throughout the phase space more energetically favorable, or energetically unlikely.

Effects of oxygen concentration

The role of oxygen concentration was studied by observing the probability of 2F, 3F, and 4F O atoms within the system. All structures analyzed here are again taken from the 1,944-atom AFNN MD trajectories. Fig. 4 provides a picture of how the coordination number of various oxygen sites changes as a function of stoichiometry. The axis presented in Fig. 4 represents a 2-dimensional histogram of the PCA space. Within each histogram bin lives configurations of atoms present in the phase space. For each structure, the amount of 2F, 3F, and 4F present in the bin and are represented by the colors in Fig. 4. A Hermite interpolation scheme [60] is used to smooth the boundaries of each histogram bin to provide a more continuous color gradient.

From Fig. 4 one can observe that the amount of 2F coordinated oxygen present in a system is highly correlated with the oxygen concentration with a roughly linear relationship existing between the oxygen concentration and 2F oxygen probability (as O concentration goes down, 2FO's probability of existing goes down). As seen in Fig. 4 (a) 2F O sites exist more frequently throughout the structure at TiO_2 when compared to $TiO_{1.85}$. This decrease is quantified by observing the change in average probability along the x-axis, where $P(TiO_2) = 30\%$ and $P(TiO_{1.85}) = 23\%$. The amount of 4F O atoms is also correlated with the oxygen concentration, with a linear trend existing between the two, as seen in Fig. 4 (c). Here, for the case of 4F O atoms, $P(TiO_2) = 9\%$ and $P(TiO_{1.85}) = 12\%$. Based on the results shown in Fig. 4 (b) there is no apparent correlation between the oxygen concentration and the amount of 3F O present within the system.

The concentrations of the various O sites can also be used to verify the NMR results obtained by experiments. As stated previously, quantification analysis of the experimental peak areas reveals fractions of 14.78%, 39.15%, and 14.68%. for 2F, 3F, and 4F O respectively. These fractions, when combined with the probabilities in Fig. 4, indicate that the experimental sample could be slightly oxygen reduced. We emphasize here that the analysis shown in Fig. 4 can be used in conjunction with experiments to aid in the validation of the characterization of the sample.

We also note that the spatial connectivity of coordination networks (ex: the connected network of 2F oxygen atoms within some volume) appears to be stoichiometry dependant, a point which will be discussed in more detail in the following sections. This implies that one could tailor the connectivity of the potentially long-range coordination networks simply by reducing the oxygen content within the sample. However, we emphasize that while the trend in 2F and 4F ratios as a function of stoichiometry appears linear up to $TiO_{1.85}$, we do not explore samples with $x < 1.85$, and therefore cannot make assertions regarding this regime.

Hydrogen binding energies

Using the 96 atom AFNN MD configurations a VGOP was calculated for each structure. Then for the first 2 PCA components of the VGOP features, K-means clustering was performed using 25 initial centroid placements. Once optimized, each point in the PCA space, which again represents an entire amorphous configuration, was binned into the corresponding K-means cluster. Stochastic random sampling was then used to down-select points from each cluster until the desired number of configurations was chosen. During the first pass, each K-means bin had the same number of points sampled from them. In the event that a cluster did not have the requested number of points, all points were taken. During the second pass the remaining number of requested points were evenly divided into each remaining cluster. This process was repeated until the total number of points requested had been chosen.

We computed H binding energies for the down-selected a-TiO_2 and a-$TiO_{1.88}$ structures (approximately 15,000 configurations), described in the previous section, to understand how hydrogen is incorporated in amorphous titania. Here, a neutral H atom (H^0) was used to examine its binding interaction in oxide, where the incorporated H^0 becomes one proton (H^+) absorbed on the O site and one electron reducing a nearby Ti; note that we did not assess the formation of hydride (H^-) on the Ti, since hydrogen thermodynamically prefers to exist as a proton (H^+) on the O site compared to a hydride (H^-) on the Ti site [61]. Fig. 5 provides plotted data for the case of a-TiO_2, while a-$TiO_{1.88}$ information can be found in the supplemental information. While we discuss this in detail throughout this section, we note for clarity here that the visual distinction between Fig. 5 and Fig. S7 is minute, indicating that there is little-to-no correlation between the hydrogen binding energy and stoichiometry, up to $TiO_{1.88}$.

Here we examine how the local oxygen coordination (O-Ti local networks) affects the hydrogen binding environment. Fig. 5(a) shows the relaxed hydrogen bonding geometries (H-O-Ti_n, n=[2,4]) for the 2F, 3F, and 4F coordinated O site, respectively. For the 2F coordinated O, we found that H preferentially binds to the apex of Ti-O-Ti bond normal to the Ti-O-Ti plane, whereas, for the 3F coordinated O, H-O-Ti_3 forms a sp^3-like pyramidal configuration; on the other hand, H bonding on the 4F coordinated O is highly distorted and not well characterized. The difference in preferential H bonding direction can be attributed to differences in the hybridization of oxygen for the different coordination environment and resulting spatial distribution of the lone pair electrons of O [62]. Previous DFT studies have demonstrated that there are two lone pairs (which are continuously distributed near the apex of Ti-O-Ti bond) for the 2F oxygen and only one lone pair for 3F, by visualizing their electron localization function. This is also consistent with earlier theoretical study reporting that hydrogen (proton) bonding to O for oxygen-containing molecules tends to lie in the directions of the lone pair orbitals [63].

Fig. 5(b) demonstrates the distribution of H binding energies (E_b) for each O CN in a-TiO_2. The E_b is calculated as follows: $E_b = E(\text{a-TiO}_x/\text{ H}) - E(\text{a-TiO}_x) - \frac{1}{2} E(H_2)$, where E(a-$TiO_x$/H) and E(a-$TiO_x$) represent total energies of a-TiO_x (x = 2 or 1.88) with and without the H binding, respectively, while $E(H_2)$ is the energy of a hydrogen gas molecule. This definition implies that a lower binding energy results in a stronger H binding.

As shown in Fig. 5(b), the E_b is strongly dependent on the O CN and H preferentially binds to lower coordinated O sites; the lower the E_b gives the stronger H binding. Given that two lone pairs for the 2F O and one lone pair for the 3F O, stronger H binding for the 2F O could be partly attributed to a higher lone pair electron density. The fitted distributions provide us with expected values for each CN site. For the case of TiO_2 we see E_b of (2F) -0.47 eV, (3F) 0.03 eV, and (4F) 0.51 eV. For the case of $TiO_{1.88}$ we obtain E_b of (2F) -0.36 eV, (3F) 0.04 eV, and (4F) 0.49 eV. These values indicate that there is little-to-no difference in the binding energy when moving to a system with a lower oxygen concentration. This implies that the

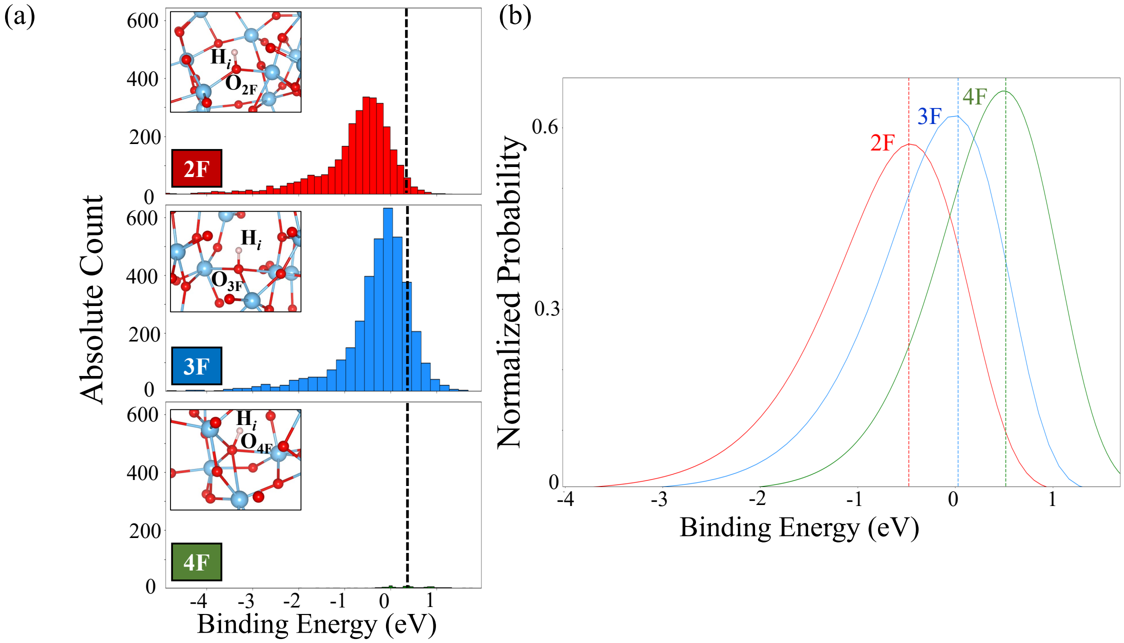

Figure 5: (a) Histograms of the hydrogen binding energies for the various CN environments. Values shown here are the absolute number of samples, signifying the significant reduction in data set size for 4F environments. Values are color coded based on the CN environment. The dashed vertical lines indicate the mean for the distributions. (b) Fitted hydrogen binding energies for TiO_2. The fits were obtained using a powernorm distribution as part of the SciPy package [57]. The distributions are colored according to the coordination number of the particular oxygen site. Here, the x-axis represents the binding energy, while the y-axis represents the probability of that binding energy occurring with respect to the number of environments for that CN type. The dashed black line represents the hydrogen binding energy in crystalline rutile. Inserted images in (a) show the oxygen environments encountered by hydrogen in the amorphous TiO_2 phase space.

electronic structure of the local oxygen environment remains similar when reducing the oxygen content in the system. It is possible that this trend continues to system with even lower oxygen concentrations, though a thorough investigation of such systems is not performed in this work.

Our computed E_b values include both proton binding on the oxygen site that is strongly dependent on the oxygen CN and electron localization energy on the Ti site that is largely determined by the lowest unoccupied electron state in the system (a-TiO_x). Thus, the variation of E_b is mostly associated with the proton binding energy on the O site, while the electron localization energy is nearly identical within the same model structure.

Finally, the E_b in rutile is calculated to be 0.29 eV for comparison, which suggests that the H binding in rutile is much weaker than the majority of H binding in a-TiO_2. Although O in rutile is 3F coordinated similar to that in a-TiO_2, the weaker H binding in rutile could be explained by the higher strain energy cost to form a sp^3-like pyramidal configuration as well as the smaller electron localization energy in rutile compared to that in a-TiO_2. Note that for a single excess electron, the computed energy difference between the small polaron and delocalized electron configuration is around 0.1 eV for rutile, which agrees well with previous calculation [64]. However, this value is much smaller than the energy gain by forming a small polaron configuration in a-TiO_2 for an excess electron, which can be as large as 0.8 eV from our calculations. We also provide binding energy values for single H within 216 atom unit cells in the supplementary information, to examine the effects of hydrogen concentration on the binding energy.

Hydrogen hopping kinetics

The results in Fig. 6 paint an interesting picture in which there are two possible physical long-range diffusion pathways present within the amorphous phase. The first exists when hydrogen is bonded to an oxygen atom and hops to another oxygen atom with a higher CN. As the binding energy distributions for the higher CN represent a more energetically unfavorable atomic environment. This disparity manifests itself as an increased likelihood that the hop will be higher in energy than that of a transition between similar CN environments, which represents option 2. This can be seen in Fig. 6 (e) where the 2F:2F hop is approximately 0.1 eV lower than the 2F:3F hop. The average activation energy for the 2F:2F hop is approximately 0.74 eV, and the average hopping barrier for 2F:3F is 0.83 eV. We note that this is not a perfect answer to the question of diffusion as there exist many higher energy 2F:2F hops than 2F:3F, implying that there exist a deeper understanding of the local atomic environments that is not captured in this work. We also note that the probability of a specific hopping pathway occurring is temperature-dependent, with lower temperatures kinetically locking the 2F:3F pathway more frequently than the 2F:2F pathway.

The existence of these two pathway types also likely depends on the ratio of coordination environments within the system. For example, if there are too few 2F sites due to a change in stoichiometry, it is possible that diffusion between 3F and 4F would occur more frequently. However, when one has a stoichiometric structure with an abundance of 2FO, it is likely that there could exist a superhighway of connected 2F environments that stretches long distances, allowing for fast diffusion through the amorphous phase. This notion is supported by the ratios observed in Fig. 4, which clearly suggests that the amount of 2F and 4F oxygen in the system strongly depends on the stoichiometry.

We again note that this effect would be temperature dependent with a limited window for 2F:2F to dominate over 2F:3F due to the similar activation barriers. We speculate that if one wished to mitigate corrosion initiation, assuming fast-travel through the amorphous phase accelerates the onset of corrosion, one could tailor both the chemistry and temperature of the system to prolong the materials lifetime by accessing higher energy kinetic pathways as hydrogen moves through the material. While we only report the kinetics of 2F:2F and 2F:3F hops in this work, we speculate that a full and thorough analysis of the nine hopping pathways between the CN environments would elucidate a better understand of how to control corrosion onset, which we leave for future work.

Conclusion

The corrosion of materials in a multitude of environments presents a significant economic and technological burden. This work aims to understand the atomic-level precursor processes that lead to the eventual failure

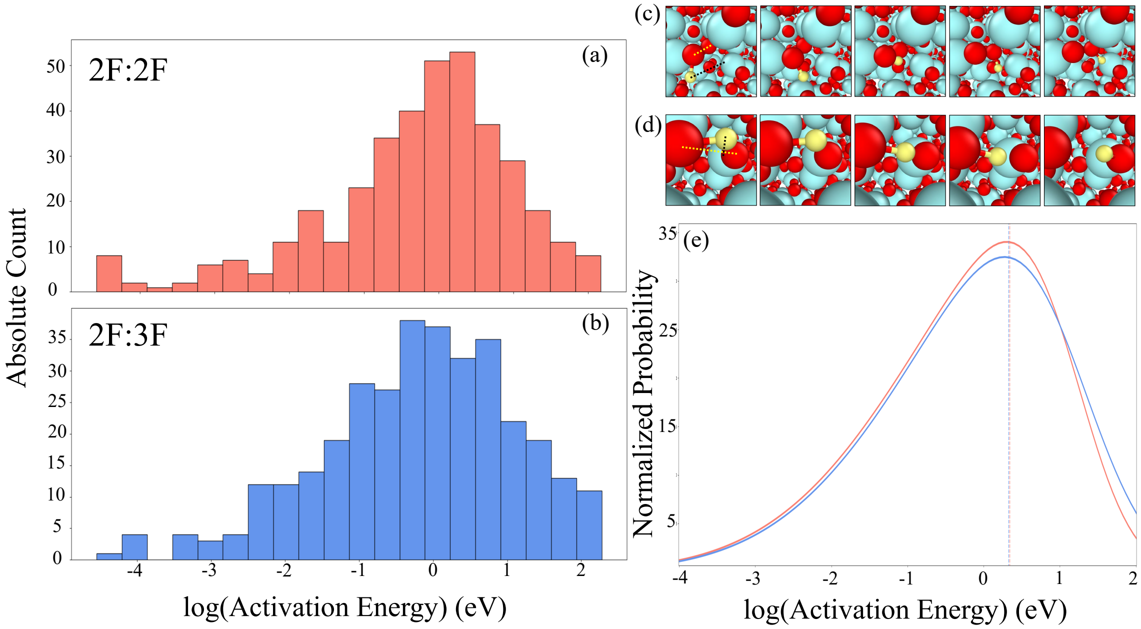

Figure 6: (a) Hydrogen hopping potential energy barriers for 2F:2F hops, where the initial and final oxygen atom was 2F coordinated. (b) Hydrogen hopping potential energy barriers for 2F:3F hops, where the initial oxygen atom was 2F coordinated and final oxygen atom was 3F coordinated. (c) Visualization of a 2F:2F hop, with red, blue, and yellow atoms representing oxygen, titanium, and hydrogen respectively. (d) Visualization of a 2F:3F hop. (e) Fitted curves (skewnorm fit) to the data shown in (a) and (b), with the line colors following the histogram colors in (a) and (b). Vertical dashed lines represent the mean of the distribution fit for each of type. In (c) and (d) there exists two guiding lines to aid in following the H diffusion pathway. The yellow line corresponds to the initial and final oxygen atoms that the H atom is bonded to throughout the pathway, while the black line shows the approximate linear pathway between the initial and final H spatial locations. Note however, that the H pathway is not linear and this line merely serves as a visual guide.

of metals and metal alloys by characterizing the structural and thermodynamic properties of hydrogen within amorphous titania. Through a combination of simulation and experiments, we can connect and validate the atomic structure of amorphous titania. We quantify the type of oxygen site based on its corresponding coordination number using NMR simulations, which is validated by experiments. Through molecular dynamics and graph theory we see that the amount of various O CN environments are stoichiometry-dependant, which is used to validate the experimental characterization using NMR.

We show through DFT calculations that hydrogen preferentially binds to 2F coordinated oxygen atoms across several stoichiometries. We also provide evidence that each O CN environment exhibits a spectrum of H binding energies, implying that not all n-fold CN environments are created equal. The H binding energies, combined with the stoichiometry-dependant rations of the various O CN environments, paints a picture where H diffusion can be affected by both the local oxygen energetics as well as the spatial properties of long-range CN networks. Hydrogen hopping kinetics were then calculated with regards to these coordination environments, showing a clear difference in activation energy depending on which coordination environment the hydrogen starts and ends at. This implies that hydrogen diffusion in amorphous titania could be controlled simply by tailoring the amount of oxygen present within the system. The tools and analysis presented in this work provide a simple and straightforward pathway to potentially understand the atomistic mechanisms behind properties such as incubation time, permeation, and ultimately corrosive failure of the underlying material.

CRediT

J. Chapman: Conceptualization, Data curation, Formal Analysis, Methodology, Software, Validation, Visualization, Writing-original draft, Writing-review and editing, K. E. Kweon: Conceptualization, Data curation, Formal Analysis, Methodology, Validation, Visualization, Writing-original draft, Writing-review and editing, Y. Zhu: Conceptualization, Data curation, Formal Analysis, Methodology, Validation, Visualization, Writing-original draft, Writing-review and editing, K. Bushick: Data curation, Writing-review and editing, L. B. B. Aji: Supervision, Methodology, Data curation, Writing-review and editing, C. A. Colla: Supervision, Methodology, Data curation, Writing-review and editing, H. Mason: Supervision, Methodology, Data curation, Writing-review and editing, N. Goldman: Supervision, Methodology, Writing-review and editing, N. Keilbart: Writing-review and editing, R. S. Qiu: Project administration, Writing-review and editing, T. W. Heo: Project administration, Writing-review and editing, J. Rodriguez: Project administration, Writing-review and editing, B. C. Wood: Project administration, Writing-original draft, Writing-review and editing

Specific Author Contributions

J. Chapman constructed the AFNN model and performed all AFNN simulations. K. Kweon generated DFT-MD data. K. Kweon performed all DFT binding energy calculations. K. Kweon and K. Bushick performed all DFT-NMR calculations. J. Chapman performed all DFT-NEB hydrogen hopping calculations. J. Chapman performed all graph characterization calculations. J. Chapman created and executed the automated hydrogen insertion pipeline. Y. Zhu conceptualized and performed all experimental measurements with the help of R. Qiu, L. Aji, C. Colla., H. Mason, and J. Rodriguez. J. Chapman, K. Kweon, Y. Zhu, and B. Wood wrote the manuscript with inputs from all authors.

Data Availability

The TiO_x AFNN created and used in this work will be included as part of the LAMMPS distribution. Several representative atomic structures can be found as part of the supplemental information. All data can be accessed upon request.

Acknowledgements

J. Chapman, K. E. Kweon, N. Goldman, N. Keilbart, Y. Zhu, C. Colla, H. Mason, R. Qiu, T. W. Heo, J. Rodriguez, and B. Wood are partially supported by the Laboratory Directed Research and Development (LDRD) program (20-SI-004) at Lawrence Livermore National Laboratory. This work was performed under the auspices of the US Department of Energy by Lawrence Livermore National Laboratory under contract No. DE-AC52-07NA27344. K.Bushick acknowledges that this material is based upon work supported by the U.S. Department of Energy, Office of Science, Office of Advanced Scientific Computing Research, Department of Energy Computational Science Graduate Fellowship under Award Number DE-SC0020347. J. Chapman gratefully acknowledges the support of the College of Engineering and Department of Mechanical Engineering at Boston University.

Supporting Information

This work contains supplemental information which can be found online.

Conflicts of Interest

There are no conflicts of interest to declare.

References

1. Vachtsevanos, G., Natarajan, K. A., Rajamanai, R. & Sandborn, P. *Corrosion processes: sensing, monitoring, data analytics, prevention/protection, diagnosis/prognosis and maintenance strategies* (Springer, 2020).
2. Gany, A. & Netzer, D. Fuel Performance Evaluation for the Solid-Fueled Ramjet. *International Journal of Turbo and Jet Engines* **2,** 157–168. `https://doi.org/10.1515/TJJ.1985.2.2.157` (1985).
3. Ewing, R. C., Runde, W. & Albrecht-Schmitt, T. E. Environmental impact of the nuclear fuel cycle: Fate of actinides. *MRS Bulletin* **35,** 859–866 (2010).
4. Schmuki, P. From Bacon to barriers: a review on the passivity of metals and alloys. *Journal of Solid State Electrochemistry* **6,** 145–164 (2002).
5. Kofstad, P. Defects and transport properties of metal oxides. *Oxidation of Metals* **44,** 3–27 (1995).
6. Kajita, S., Minato, T., Kato, H. S., Kawai, M. & Nakayama, T. First-principles calculations of hydrogen diffusion on rutile TiO2(110) surfaces. *The Journal of Chemical Physics* **127,** 104709. eprint: `https://doi.org/10.1063/1.2768951`. `https://doi.org/10.1063/1.2768951` (2007).
7. Zhang, H. & F. Banfield, J. Thermodynamic analysis of phase stability of nanocrystalline titania. *J. Mater. Chem.* **8,** 2073–2076. `http://dx.doi.org/10.1039/A802619J` (9 1998).
8. Henrich, V. E. & Kurtz, R. L. Surface electronic structure of TiO2: Atomic geometry, ligand coordination, and the effect of adsorbed hydrogen. *Physical Review B* **23,** 6280–6287 (1981).
9. Merinov, B. & Goddard, W. Proton diffusion pathways and rates in Y-doped BaZrO3 solid oxide electrolyte from quantum mechanics. *The Journal of Chemical Physics* **130,** 194707. eprint: `https://doi.org/10.1063/1.3122984`. `https://doi.org/10.1063/1.3122984` (2009).
10. Lu, G. & Kaxiras, E. Hydrogen Embrittlement of Aluminum: The Crucial Role of Vacancies. *Physical Review Letters* **94** (2005).
11. Nickel, N. H., Johnson, N. M. & Jackson, W. B. Hydrogen passivation of grain boundary defects in polycrystalline silicon thin films. *Applied Physics Letters* **62,** 3285–3287. eprint: `https://doi.org/10.1063/1.109101`. `https://doi.org/10.1063/1.109101` (1993).

12. Wang, F., Lai, W., Li, R., He, B. & Li, S. Fast hydrogen diffusion along the $\Sigma 7$ grain boundary of α-Al2O3: A first-principles study. *International Journal of Hydrogen Energy* **41,** 22214–22220. ISSN: 0360-3199. `https://www.sciencedirect.com/science/article/pii/S0360319916328865` (2016).
13. Zhu, Y. *et al.* Hydriding of titanium: Recent trends and perspectives in advanced characterization and multiscale modeling. *Current Opinion in Solid State and Materials Science,* 101020. ISSN: 1359-0286. `https://www.sciencedirect.com/science/article/pii/S1359028622000407` (2022).
14. Keblinski, P., Phillpot, S., Wolf, D. & Gleiter, H. Amorphous structure of grain boundaries and grain junctions in nanocrystalline silicon by molecular-dynamics simulation. *Acta Materialia* **45,** 987–998. ISSN: 1359-6454. `https://www.sciencedirect.com/science/article/pii/S1359645496002364` (1997).
15. Franc, J.-P. Incubation Time and Cavitation Erosion Rate of Work-Hardening Materials. *Journal of Fluids Engineering* **131.** 021303. ISSN: 0098-2202. eprint: `https://asmedigitalcollection.asme.org/fluidsengineering/article-pdf/131/2/021303/5837171/021303\_1.pdf`. `https://doi.org/10.1115/1.3063646` (Jan. 2009).
16. Song, F. Predicting the mechanisms and crack growth rates of pipelines undergoing stress corrosion cracking at high pH. *Corrosion Science* **51,** 2657–2674. ISSN: 0010-938X. `https://www.sciencedirect.com/science/article/pii/S0010938X09003254` (2009).
17. Kamrunnahar, M. & Urquidi-Macdonald, M. Prediction of corrosion behavior using neural network as a data mining tool. *Corrosion Science* **52,** 669–677. ISSN: 0010-938X. `https://www.sciencedirect.com/science/article/pii/S0010938X09005071` (2010).
18. El Maaddawy, T. & Soudki, K. A model for prediction of time from corrosion initiation to corrosion cracking. *Cement and Concrete Composites* **29,** 168–175. ISSN: 0958-9465. `https://www.sciencedirect.com/science/article/pii/S0958946506001971` (2007).
19. Yashima, M. Invited Review: Some recent developments in the atomic-scale characterization of structural and transport properties of ceria-based catalysts and ionic conductors. *Catalysis Today* **253.** Catalysis by ceria, 3–19. ISSN: 0920-5861. `https://www.sciencedirect.com/science/article/pii/S0920586115002035` (2015).
20. Andersson, M., Yuan, J. & Sundén, B. Review on modeling development for multiscale chemical reactions coupled transport phenomena in solid oxide fuel cells. *Applied Energy* **87,** 1461–1476. ISSN: 0306-2619. `https://www.sciencedirect.com/science/article/pii/S0306261909005005` (2010).
21. Sun, C., Hui, R. & Roller, J. Cathode materials for solid oxide fuel cells: a review. *Journal of Solid State Electrochemistry* **14,** 1125–1144. ISSN: 1433-0768. `https://doi.org/10.1007/s10008-009-0932-0` (July 2010).
22. Kärger, J. & Ruthven, D. M. Diffusion in nanoporous materials: fundamental principles, insights and challenges. *New J. Chem.* **40,** 4027–4048. `http://dx.doi.org/10.1039/C5NJ02836A` (5 2016).
23. Getman, R. B., Bae, Y.-S., Wilmer, C. E. & Snurr, R. Q. Review and Analysis of Molecular Simulations of Methane, Hydrogen, and Acetylene Storage in Metal–Organic Frameworks. *Chemical Reviews* **112.** PMID: 22188435, 703–723. eprint: `https://doi.org/10.1021/cr200217c`. `https://doi.org/10.1021/cr200217c` (2012).
24. Kresse, G. & Furthmüller, J. Efficiency of ab-initio total energy calculations for metals and semiconductors using a plane-wave basis set. *Computational Materials Science* **6,** 15–50. ISSN: 0927-0256. `https://www.sciencedirect.com/science/article/pii/0927025696000080` (1996).
25. Blöchl, P. E. Projector augmented-wave method. *Phys. Rev. B* **50,** 17953–17979. `https://link.aps.org/doi/10.1103/PhysRevB.50.17953` (24 Dec. 1994).
26. Perdew, J. P. *et al.* Restoring the Density-Gradient Expansion for Exchange in Solids and Surfaces. *Phys. Rev. Lett.* **100,** 136406. `https://link.aps.org/doi/10.1103/PhysRevLett.100.136406` (13 Apr. 2008).

27. Cui, Z.-H., Wu, F. & Jiang, H. First-principles study of relative stability of rutile and anatase TiO2 using the random phase approximation. *Phys. Chem. Chem. Phys.* **18,** 29914–29922. `http://dx.doi.org/10.1039/C6CP04973G` (43 2016).

28. Mavračić, J., Mocanu, F. C., Deringer, V. L., Csányi, G. & Elliott, S. R. Similarity Between Amorphous and Crystalline Phases: The Case of TiO2. *The Journal of Physical Chemistry Letters* **9.** PMID: 29763315, 2985–2990. eprint: `https://doi.org/10.1021/acs.jpclett.8b01067`. `https://doi.org/10.1021/acs.jpclett.8b01067` (2018).

29. Yang, K. *et al.* New insights into the atomic structure of amorphous TiO2 using tight-binding molecular dynamics. *The Journal of Chemical Physics* **149,** 094501. eprint: `https://doi.org/10.1063/1.5042783`. `https://doi.org/10.1063/1.5042783` (2018).

30. Li, X. *et al.* Cooling rate effects in sodium silicate glasses: Bridging the gap between molecular dynamics simulations and experiments. *The Journal of Chemical Physics* **147,** 074501. eprint: `https://doi.org/10.1063/1.4998611`. `https://doi.org/10.1063/1.4998611` (2017).

31. Dingwell, D. B. The Density of Titanium(IV) Oxide Liquid. *Journal of the American Ceramic Society* **74,** 2718–2719. eprint: `https://ceramics.onlinelibrary.wiley.com/doi/pdf/10.1111/j.1151-2916.1991.tb06833.x`. `https://ceramics.onlinelibrary.wiley.com/doi/abs/10.1111/j.1151-2916.1991.tb06833.x` (1991).

32. Alderman, O. L. G., Skinner, L. B., Benmore, C. J., Tamalonis, A. & Weber, J. K. R. Structure of molten titanium dioxide. *Phys. Rev. B* **90,** 094204. `https://link.aps.org/doi/10.1103/PhysRevB.90.094204` (9 Sept. 2014).

33. Ashbrook, S. E. & McKay, D. Combining solid-state NMR spectroscopy with first-principles calculations – a guide to NMR crystallography. *Chem. Commun.* **52,** 7186–7204. `http://dx.doi.org/10.1039/C6CC02542K` (45 2016).

34. Wang, M. *et al.* Identification of different oxygen species in oxide nanostructures with ¡sup¿17¡/sup¿O solid-state NMR spectroscopy. *Science Advances* **1,** e1400133. eprint: `https://www.science.org/doi/pdf/10.1126/sciadv.1400133`. `https://www.science.org/doi/abs/10.1126/sciadv.1400133` (2015).

35. Li, Y. *et al.* Distinguishing faceted oxide nanocrystals with 17O solid-state NMR spectroscopy. *Nature Communications* **8,** 581. ISSN: 2041-1723. `https://doi.org/10.1038/s41467-017-00603-7` (Sept. 2017).

36. Pascual-Borràs, M., López, X., Rodríguez-Fortea, A., Errington, R. J. & Poblet, J. M. 17O NMR chemical shifts in oxometalates: from the simplest monometallic species to mixed-metal polyoxometalates. *Chem. Sci.* **5,** 2031–2042. `http://dx.doi.org/10.1039/C4SC00083H` (5 2014).

37. Bastow, T. J., Moodie, A. F., Smith, M. E. & Whitfield, H. J. Characterisation of titania gels by 17O nuclear magnetic resonance and electron diffraction. *J. Mater. Chem.* **3,** 697–702. `http://dx.doi.org/10.1039/JM9930300697` (7 1993).

38. Dudarev, S. L., Botton, G. A., Savrasov, S. Y., Humphreys, C. J. & Sutton, A. P. Electron-energy-loss spectra and the structural stability of nickel oxide: An LSDA+U study. *Phys. Rev. B* **57,** 1505–1509. `https://link.aps.org/doi/10.1103/PhysRevB.57.1505` (3 Jan. 1998).

39. Finazzi, E., Di Valentin, C., Pacchioni, G. & Selloni, A. Excess electron states in reduced bulk anatase TiO2: Comparison of standard GGA, GGA+U, and hybrid DFT calculations. *The Journal of Chemical Physics* **129,** 154113. eprint: `https://doi.org/10.1063/1.2996362`. `https://doi.org/10.1063/1.2996362` (2008).

40. Arroyo-de Dompablo, M. E., Morales-García, A. & Taravillo, M. DFT+U calculations of crystal lattice, electronic structure, and phase stability under pressure of TiO2 polymorphs. *The Journal of Chemical Physics* **135,** 054503. eprint: `https://doi.org/10.1063/1.3617244`. `https://doi.org/10.1063/1.3617244` (2011).

41. Curnan, M. T. & Kitchin, J. R. Investigating the Energetic Ordering of Stable and Metastable TiO2 Polymorphs Using DFT+U and Hybrid Functionals. *The Journal of Physical Chemistry C* **119,** 21060–21071. eprint: `https://doi.org/10.1021/acs.jpcc.5b05338`. `https://doi.org/10.1021/acs.jpcc.5b05338` (2015).

42. Henkelman, G., Uberuaga, B. P. & Jónsson, H. A climbing image nudged elastic band method for finding saddle points and minimum energy paths. *The Journal of Chemical Physics* **113,** 9901–9904. eprint: `https://doi.org/10.1063/1.1329672`. `https://doi.org/10.1063/1.1329672` (2000).

43. Chapman, J. & Ramprasad, R. Multiscale Modeling of Defect Phenomena in Platinum Using Machine Learning of Force Fields. *JOM* **72,** 4346–4358. ISSN: 1543-1851. `https://doi.org/10.1007/s11837-020-04385-0` (Dec. 2020).

44. Chapman, J., Batra, R. & Ramprasad, R. Machine learning models for the prediction of energy, forces, and stresses for Platinum. *Computational Materials Science* **174,** 109483. ISSN: 0927-0256. `https://www.sciencedirect.com/science/article/pii/S0927025619307827` (2020).

45. Liut, D. A., Matheu, E. E., Singh, M. P. & Mook, D. T. Neural-network control of building structures by a force-matching training scheme. *Earthquake Engineering & Structural Dynamics* **28,** 1601–1620 (1999).

46. Likas, A., Vlassis, N. & J. Verbeek, J. The global k-means clustering algorithm. *Pattern Recognition* **36.** Biometrics, 451–461. ISSN: 0031-3203. `https://www.sciencedirect.com/science/article/pii/S0031320302000602` (2003).

47. Bera, S. & Shrivastava, V. K. Analysis of various optimizers on deep convolutional neural network model in the application of hyperspectral remote sensing image classification. *International Journal of Remote Sensing* **41,** 2664–2683. eprint: `https://doi.org/10.1080/01431161.2019.1694725`. `https://doi.org/10.1080/01431161.2019.1694725` (2020).

48. Plimpton, S. Fast parallel algorithms for short-range molecular dynamics. *J. Compu. Phys.* **117,** 1–19. ISSN: 0021-9991. `http://lammps.sandia.gov/` (1995).

49. Chapman, J., Goldman, N. & Wood, B. C. Efficient and universal characterization of atomic structures through a topological graph order parameter. *npj Computational Materials* **8,** 37. ISSN: 2057-3960. `https://doi.org/10.1038/s41524-022-00717-7` (Mar. 2022).

50. Borghols, W. J. H. *et al.* Lithium Storage in Amorphous TiO[sub 2] Nanoparticles. *Journal of The Electrochemical Society* **157,** A582. `https://doi.org/10.1149/1.3332806` (2010).

51. Wang, Y. *Handbook of modern Ion Beam Materials Analysis Appendices* (Materials Research Society, 2010).

52. Padayachee, J., Meyer, K. & Prozesky, V. Automatic analysis of Rutherford backscattering spectrometry spectra. *Nuclear Instruments and Methods in Physics Research Section B: Beam Interactions with Materials and Atoms* **181.** 7th International Conference on Nuclear Microprobe Technology and Applications, 122–127. ISSN: 0168-583X. `https://www.sciencedirect.com/science/article/pii/S0168583X01005377` (2001).

53. Sen-Britain, S. T. *et al.* Transformations of Ti-5Al-5V-5Cr-3Mo powder due to reuse in laser powder bed fusion: A surface analytical approach. *Applied Surface Science* **564,** 150433. ISSN: 0169-4332. `https://www.sciencedirect.com/science/article/pii/S0169433221015063` (2021).

54. Massiot, D. *et al.* Modelling one- and two-dimensional solid-state NMR spectra. *Magnetic Resonance in Chemistry* **40,** 70–76. eprint: `https://analyticalsciencejournals.onlinelibrary.wiley.com/doi/pdf/10.1002/mrc.984`. `https://analyticalsciencejournals.onlinelibrary.wiley.com/doi/abs/10.1002/mrc.984` (2002).

55. Stukowski, A. Visualization and analysis of atomistic simulation data with OVITO–the Open Visualization Tool. *Modelling and Simulation in Materials Science and Engineering* **18,** 015012. `https://doi.org/10.1088/0965-0393/18/1/015012` (Dec. 2009).

56. Hunter, J. D. Matplotlib: A 2D graphics environment. *Computing in Science & Engineering* **9,** 90–95 (2007).

57. Virtanen, P. *et al.* SciPy 1.0: Fundamental Algorithms for Scientific Computing in Python. *Nature Methods* **17,** 261–272 (2020).

58. Pedregosa, F. *et al.* Scikit-learn: Machine Learning in Python. *Journal of Machine Learning Research* **12,** 2825–2830 (2011).

59. Day, V. W., Eberspacher, T. A., Klemperer, W. G., Park, C. W. & Rosenberg, F. S. Solution structure elucidation of early transition metal polyoxoalkoxides using oxygen-17 NMR spectroscopy. *Journal of the American Chemical Society* **113,** 8190–8192. eprint: `https://doi.org/10.1021/ja00021a068`. `https://doi.org/10.1021/ja00021a068` (1991).

60. de Boor, C., Höllig, K. & Sabin, M. High accuracy geometric Hermite interpolation. *Computer Aided Geometric Design* **4,** 269–278. ISSN: 0167-8396. `https://www.sciencedirect.com/science/article/pii/0167839687900021` (1987).

61. Hu, G., Wu, Z. & Jiang, D.-e. First Principles Insight into H2 Activation and Hydride Species on TiO2 Surfaces. *The Journal of Physical Chemistry C* **122,** 20323–20328. eprint: `https://doi.org/10.1021/acs.jpcc.8b05251`. `https://doi.org/10.1021/acs.jpcc.8b05251` (2018).

62. Muscenti, T. M., Gibbs, G. & Cox, D. F. A simple chemical view of relaxations at stoichiometric (110) surfaces of rutile-structure type oxides: A first-principles study of stishovite, SiO2. *Surface Science* **594,** 70–82. ISSN: 0039-6028. `https://www.sciencedirect.com/science/article/pii/S0039602805008228` (2005).

63. Murray-Rust, P. & Glusker, J. P. Directional hydrogen bonding to sp2- and sp3-hybridized oxygen atoms and its relevance to ligand-macromolecule interactions. *Journal of the American Chemical Society* **106,** 1018–1025. eprint: `https://doi.org/10.1021/ja00316a034`. `https://doi.org/10.1021/ja00316a034` (1984).

64. Janotti, A., Franchini, C., Varley, J. B., Kresse, G. & Van de Walle, C. G. Dual behavior of excess electrons in rutile TiO2. *physica status solidi (RRL) – Rapid Research Letters* **7,** 199–203. eprint: `https://onlinelibrary.wiley.com/doi/pdf/10.1002/pssr.201206464`. `https://onlinelibrary.wiley.com/doi/abs/10.1002/pssr.201206464` (2013).